Titre: Title:	Cislunar communication performance and system analysis with uncharted phenomena
Auteurs: Authors:	Selen Gecgel Cetin, Angeles Vázquez-Castro, & Gunes Karabulut Kurt
Date:	2024
Type:	Article de revue / Article
Référence: Citation:	Gecgel Cetin, S., Vázquez-Castro, A., & Karabulut Kurt, G. (2024). Cislunar communication performance and system analysis with uncharted phenomena. IEEE Open Journal of the Communications Society, 5, 6404-6419. https://doi.org/10.1109/ojcoms.2024.3474571

Document en libre accès dans PolyPublie
Open Access document in PolyPublie

URL de PolyPublie: PolyPublie URL:	https://publications.polymtl.ca/59618/
Version:	Version officielle de l'éditeur / Published version Révisé par les pairs / Refereed
Conditions d'utilisation: Terms of Use:	CC BY

Document publié chez l'éditeur officiel
Document issued by the official publisher

Titre de la revue: Journal Title:	IEEE Open Journal of the Communications Society (vol. 5)
Maison d'édition: Publisher:	IEEE Communications Society
URL officiel: Official URL:	https://doi.org/10.1109/ojcoms.2024.3474571
Mention légale: Legal notice:	©2024 The Authors. This work is licensed under a Creative Commons Attribution 4.0 License. For more information, see https://creativecommons.org/licenses/by/4.0/

Cislunar Communication Performance and System Analysis With Uncharted Phenomena

SELEN GECGEL CETIN[1,2] **(Member, IEEE), ÁNGELES VAZQUEZ-CASTRO**[3] **(Senior Member, IEEE), AND GUNES KARABULUT KURT**[2] **(Senior Member, IEEE)**

[1]Department of Electronics and Communication Engineering, Istanbul Technical University, 34469 Istanbul, Türkiye

[2]Department of Electrical Engineering, Polytechnique Montréal, Montreal, QC H3T 1J4, Canada

[3]Department of Telecommunications and Systems Engineering, Autonomous University of Barcelona, 08193 Barcelona, Spain

CORRESPONDING AUTHOR: S. GECGEL CETIN (e-mail: gecgel16@itu.edu.tr)

ABSTRACT The Moon and its surrounding cislunar space have numerous unknowns, uncertainties, or partially charted phenomena that need to be investigated to determine the extent to which they affect cislunar communication. These include temperature fluctuations, spacecraft distance and velocity dynamics, surface roughness, and the diversity of propagation mechanisms. To develop robust and dynamically operative Cislunar space networks (CSNs), we need to analyze the communication system by incorporating inclusive models that account for the wide range of possible propagation environments and noise characteristics. In this paper, we consider that the communication signal can be subjected to both Gaussian and non-Gaussian noise, but also to different fading conditions. First, we analyze the communication link by showing the relationship between the brightness temperatures of the Moon and the equivalent noise temperature at the receiver of the Lunar Gateway. We propose to analyze the ergodic capacity and the outage probability, as they are essential metrics for the development of reliable communication. In particular, we model the noise with the additive symmetric alpha-stable distribution, which allows a generic analysis for Gaussian and non-Gaussian signal characteristics. Then, we present the closed-form bounds for the ergodic capacity and the outage probability. Finally, the results show the theoretically and operationally achievable performance bounds for the cislunar communication. To give insight into further designs, we also provide our results with comprehensive system settings that include mission objectives as well as orbital and system dynamics.

INDEX TERMS Blahut-Arimoto, brightness temperature, cislunar space networks, lunar communication, lunar gateway, non-Gaussian, symmetric alpha-stable distribution, temperature fluctuations.

I. INTRODUCTION

MOON is coming to the fore with long-term and advanced goals, not least due to the involvement of new players on the commercial side [1], [2], [3]. Lunar missions with economic and scientific objectives increase, but also emerge as precursors of deep space missions and expand the scope [4], [5], [6]. For example, the Artemis Base Camp, the surface habitation on the Moon, is being planned under the leadership of NASA and will also be used for missions to Mars [7]. The catalysis of commercial and national actors accelerates a thriving progress to build cislunar space networks (CSNs) for potential users in space such as astronauts, crew exploration vehicles, robotic rovers and crewmember landers [8]. CSNs provide communication, navigation and tracking services and are established with relay satellites, orbiters, spacecraft, terrain vehicles and rovers [9]. All architectures for CSNs are expected to ensure end-to-end security, cross-support as well as scalability and expandability to integrate them into future CSNs [10], [11], [12]. However, the most urgent objectives for CSNs are not these, but dynamic capabilities [13] and high interoperability [14], as they are the prerequisite to successfully conduct lunar missions.

A. CISLUNAR SPACE FOR CSNs

CSNs must be designed and developed to withstand environmental conditions in cislunar space, but also to potential threats and anomalies such as solar scintillation [15], [16], [17], [18], dust storms [19], natural and artificial radiation sources [20], [21], [22], [23]. Conveying the current technologies used for communications on Earth and in near space is the main approach to develop robust and adaptable systems with high performance [12], [13], [14]. However, previous missions show the differences between cislunar and near space, but also between the Earth and the Moon, which cannot be considered identical. Scientists and engineers design lunar communication systems by simulating the systems or by using appropriate models based on the accumulated knowledge. The tough challenge is to bring the interdisciplinary knowledge together for a realistic analysis. There are still partially charted phenomena, uncertainties and unknowns that can affect communication performance or jeopardize the entire mission [24], [25], [26], [27], [28].

The unique conditions of cislunar space bring with them crucial aspects that must be considered in the development of the communication system to ensure robust and reliable communication. The physical temperatures of the Moon and Earth change daily and seasonally as they orbit around the Earth and Sun, respectively [29], [30], [31]. However, the lack of a dense atmosphere and large bodies of water as on Earth leads to strong temperature fluctuations on the Moon during the lunar day and night [32]. This inevitably affects the operation of electronic systems, even those produced with large survivability limits [33], [34], [35]. Such temperature fluctuations also pose a major challenge to the stable operation of communication systems, as the noise signals vary depending on the system temperature [36], [37], [38], [39]. This is a stark contrast with communication systems on Earth and in near space, where environmental conditions are more stable and predictable. Furthermore, due to the hilly terrain and the spherical shape of the Moon, the lunar surface is not evenly exposed to sunlight. As a result, the temperature fluctuations between sunlit and shadowed areas are complicated during the lunar day and night [40]. For example, the system temperature can change instantly and cause impulsive noises when a rover moves to another location, even at close range. This is another difference to communications on Earth and in near space, where the noise is usually assumed to be Gaussian. To provide reliable and robust communication given the dynamic nature of the cislunar environment, we should consider the presence of both non-Gaussian and Gaussian signal characteristics.

Another important aspect is the diversity of propagation mechanisms in the cislunar environment. For example, the visibility of transmission paths is uncertain due to the hilly terrain and the mobility of spacecraft and users on the surface [41], [42], [43], [44]. Thus, line-of-sight (LoS) and non-line-of-sight (NLoS) transmissions can occur individually or together. We also know that diffraction loss increases with decreasing elevation angle [44]. In addition, the multifaceted lunar surface and the varying reflectivity of the lunar regolith further complicate the scattering and reflection conditions [44], [45], [46], [47], [48], [49], [50]. However, communication systems must be developed to ensure the expected performance even under unfavorable conditions for the signal attenuation. Therefore, we should consider (at least the most probable cases) for LoS and NLoS communication with other attenuation effects such as scattering, diffraction and reflection properties.

B. RELATED WORKS AND SYSTEM CONSIDERATIONS

Aforementioned aspects of cislunar space and the corresponding suggestions emphasize the need for inclusive models that account for a wide range of propagation conditions and noise characteristics. In this way, we can design and develop robust and reliable cislunar communication systems but also dynamically adaptable to support the short- and long-term goals of lunar missions and beyond [51].

Communication systems in near space and on Earth are generally developed under the assumption of Gaussian noise. However, this may not apply to all communication scenarios, resulting in poor performance. In particular, communication in challenging environments such as cislunar space with temperature fluctuations, unstable orbital conditions [52], [53], unexpected interference and anomalies [54], [55], [56], [57], [58] that can lead to significant deviations in noise characteristics. Symmetric Alpha-Stable (SαS) distribution with its rich parameterization proves to be a well-suited model for relatively unstable systems such as power-line, underwater and cislunar communications. It enables generic analysis and adaptive development of communication systems that can operate effectively under different noise conditions, from common Gaussian noise scenarios to more extreme cases with impulsive, non-Gaussian noise. Therefore, we model the channel with additive symmetric alpha-stable noise (ASαSN) to consider both Gaussian and non-Gaussian signals.

ASαSN is usually adopted to model interference, mostly within the additive white Gaussian noise (AWGN) channel and the studies provide analyses over different performance metrics such as error rates, outage, or detection probabilities [59], [60], [61], [62], [63], [64]. There are some studies that perform analysis on ASαSN channels without Gaussian noise. In [65], the authors analyze the diversity combining schemes under Rayleigh fading and ASαSN and present the error performance with closed-form expressions for the diversity and array gains. In [66], the error performance of phase shift keying modulation is investigated using the geometric power of ASαSN variables without considering fading. However, the majority of studies focus on error performance rather than capacity or ergodic capacity. There are only a handful of studies that consider ASαSN within the basis of AWGN channel [67], [68], [69], [70], due to challenging properties of SαS variables. As far as we are aware, [71] is the first study that directly focuses on the optimization of the capacity maximization problem without system constraints or other focuses. The authors of [71] use
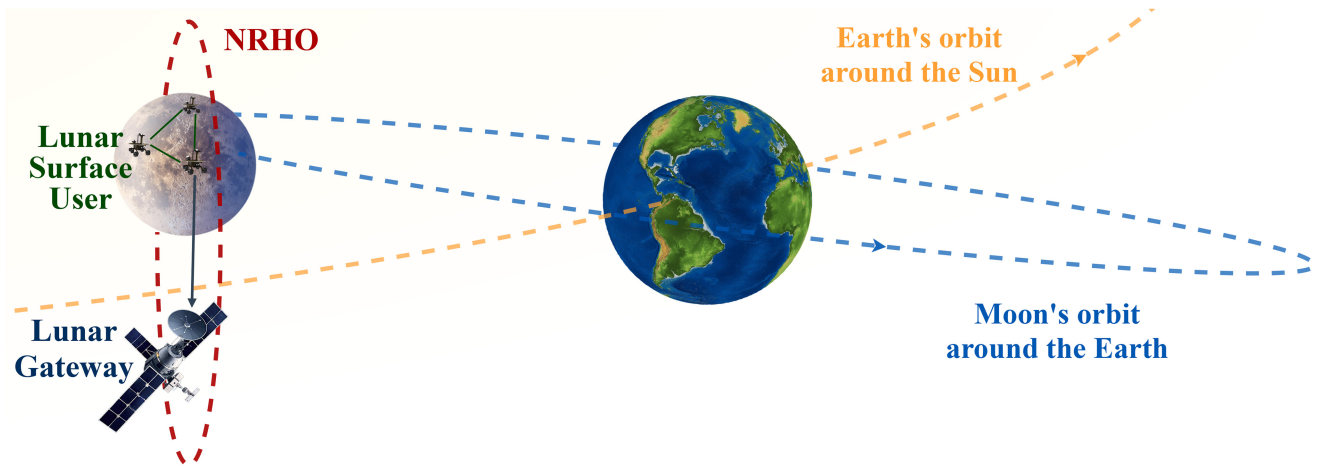
FIGURE 1. The uplink communication from the lunar surface user to the Lunar Gateway. The exaggerated view of cislunar space in which the Lunar Gateway orbits in near-rectilinear halo orbit (NRHO) while the Moon and Earth move in their orbits. One of the lunar surface users represents the communication terminal of the lunar mission and transmits information.

the generalization of Shannon's channel coding theorem for non-Gaussian channels [72] and adapt this generalization for ASαSN. In this study, we use this bound as the basis for the theoretical analyses under the Nakagami-m fading.

In the existing studies on lunar communication, the Rician fading model is usually considered, while Rayleigh fading is assumed for cases where there is no LoS, such as at low elevation angles [42], [43], [44], [45], [46], [47], [48], [49], [50]. However, all these studies focus on the direct communication link between the Earth station and the Lunar South Pole. Since the Earth and the Moon rotate at approximately the same speed, the relative movements of the transmitter and receiver do not change or are negligible. For CSNs providing services for complex missions, the situation is quite different. In particular, CSN architectures are based on relay spacecrafts moving at varying speeds in unstable lunar orbits. If we consider the cislunar spacecraft and its relative movement to the mobile user on the lunar surface, the propagation mechanisms become even more diverse. The Nakagami-m fading model is feasible to exactly or approximately represent different propagation scenarios as well as for closed-form theoretical analyses. Therefore, we performed our analyses with the Nakagami-m fading model to gain a better insight into the performance range of cislunar communication. *To the best of our knowledge, there is no study that specifically addresses capacity analysis under ASαSN and Nakagami-m fading, nor is there any study that provides an analysis of ergodic capacity and outage probability for cislunar communication with this extent.*

C. CONTRIBUTIONS

We perform all analyses via NASA's Lunar Gateway communication link, as illustrated in Fig. 1. Our main contributions are listed below.

- We highlight the critical system aspects for the design and development of CSNs but also provide insights into the potential threats and anomalies in cislunar space.

- We analyze the communication link of the foremost CSN architecture by presenting the theoretical formulation for the relationship between the brightness temperatures and the equivalent noise temperature at the receiver. In this way, we address a less unexplored aspect of communication in cislunar space.

- We provide the theoretical derivations in closed-form for the probability distribution function (pdf) of the instantaneous signal-to-noise ratio (SNR), the lower bound of the ergodic capacity and the corresponding upper bound of the outage probability for ASαSN and Nakagami-m fading, which to the best of our knowledge are presented for the first time in the literature.

- As described in Algorithm 1, we present the numerical approximation algorithm for the ergodic capacity to account for fading by adapting the Blahut-Arimoto algorithm, which to our knowledge is the first in the literature.

- We establish the direct link between environmental variations (temperature, noise and fading) in cislunar space and the corresponding performance metrics via our results.

- We extend the our results to provide realistic insights for system-level designs, which affects the choice of technologies, frequency band and power levels, as well as for mission-level considerations.

Our analyses show the obvious influence of brightness temperature under ASαSN for the S and Ka bands, which are intended for low and high data rates. The ergodic capacity decreases and the outage probability increases significantly depending on the brightness temperature for the Gaussian and non-Gaussian noise characteristics. Furthermore, our results show how much fading conditions amplify these effects under different system settings. Overall, our work provides insight into the design and optimization of future

---

Algorithm 1 Approximate Computation of Ergodic Capacity

for $i \in \{1, \ldots, N_h\}$ **do**

    (1) Initialize $r^{(0)}(x) = \frac{1}{M_X}$

    (2) Initialize $\overline{C} = 0, \ C_{i,0} = 0, \ C_{i,-1} = -2\epsilon$

    while $C_{i,n} - C_{i,n-1} > \epsilon$ **do**

        (1) $C_{i,n-1} = C_{i,n}$

        (2) $Q^{(n)}(x|y) = \frac{r^{(n-1)}(x)P(y|x)}{\sum_{x=1}^{M_X} r^{(n-1)}(x)P(y|x)}$

        (3) $C_{i,n} = \sum_{x=1}^{M_X} \sum_{y=1}^{M_N} r^{(n-1)}(x)P(y|x)$

$$\times \log_2\left(\frac{Q^{(n)}(x|y)}{r^{(n-1)}(x)}\right)$$

        (4) Solve for ν such that

$$\sum_{x=1}^{M_X}\left(1 - \frac{|x|}{P_c h_i}\right)e^{\nu|x|}\prod_{y=1}^{M_N} Q^{(n)}(x|y)^{P(y|x)} = 0 \quad (27)$$

$$r^{(n)}(x_i) = \frac{e^{\nu|x_i|}\prod_{y=1}^{M_N} Q^{(n)}(x|y)^{P(y|x)}}{\sum_{x'=1}^{M_X} e^{\nu|x'|}\prod_{y=1}^{M_N} Q^{(n)}(x'|y)^{P(y|x')}} \quad (28)$$

    end while

    return $C_{i,n}$

    (5) $\overline{C} = \overline{C} + C_{i,n}f_\gamma(\gamma_i)\Delta_i$

end for

return $\overline{C}$

---

cislunar communication systems to meet the upward trend of expected performance.

D. NOTATION AND ORGANIZATION

The rest of the article is structured as follows. The preliminaries are given in Section II. Section III presents an unified modeling framework that generalizes system and channel models by considering the conditions in cislunar space and the effect of lunar illumination. Section IV provides the theoretical analysis for the ergodic capacity and outage probability together with the numerical approximations for ergodic capacity. The system-level performance analysis is performed by integrating the theoretical analysis and the numerical results are presented in Section V. Finally, Section VI concludes the paper.

Notation: Throughout the paper, absolute value of a scalar is denoted by $|\cdot|$ and $\mathbb{E}[X]$, $F_X(x)$ and $f_X(x)$ denote the mean, the cumulative distribution function (cdf) and pdf of a random variable X. $\Gamma(\cdot)$, $\Gamma(\cdot, \cdot)$ and $G_{p,q}^{m,n}[(\cdot)|(\cdot)]$ symbolize the gamma function, the lower incomplete gamma function and the Meijer-G function.

II. PRELIMINARIES

The alpha-stable distribution, is denoted by $\mathcal{S}(\alpha, \beta, \lambda, \mu)$ where the index of the stability $\alpha \in (0, 2]$, the skewness parameter $\beta \in [-1, +1]$, the scale parameter $\lambda \in (0, +\infty)$ and the shift parameter $\mu \in (-\infty, +\infty)$ are parameters.

When $\alpha \neq 1$, the alpha-stable distribution is defined with the characteristic function as follows [73]

$$\Phi(t) = \exp\left[j\mu t - \lambda^\alpha |t|^\alpha \left(1 - j\beta\,\text{sign(t)}\tan\frac{\pi\alpha}{2}\right)\right]. \quad (1)$$

If $\beta = 0$ and $\mu = 0$, the alpha-stable distribution is called as symmetric alpha-stable (SαS) distribution, which is a generalization of Gauss distribution with zero mean and is valid in many scenarios considering signal distortions. The characteristic function of SαS distribution takes the form as follows

$$\Phi(t) = \exp\left(-\lambda^\alpha |t|^\alpha\right). \quad (2)$$

Here, we provide five properties of alpha-stable random variables that are used throughout the paper.

Property 1: Let $Z \sim S(\alpha, \beta, \lambda, \mu)$ with $\alpha \in (0, 2)$. Then,
$E[|Z|^p] < \infty$ for any $0 < p < \alpha$,
$E[|Z|^p] = \infty$ for any $p \geq \alpha$.

Property 2: Let $Z \sim S(\alpha, \beta, \lambda, \mu)$ with $\alpha \in (0, 2)$. Then, the shift parameter μ equals to the mean.

Property 3: Let $Z \sim S(\alpha, 0, \lambda, 0)$ with $\alpha \in (1, 2]$. Then,

$$\mathbb{E}[|Z|] = \frac{2\lambda\Gamma\left(1 - \frac{1}{\alpha}\right)}{\pi}. \quad (3)$$

Property 4: Let Z_1 and Z_2 independent and identically distributed (i.i.d.) variables of $Z_i \sim S(\alpha, \beta_i, \lambda_i, \mu_i)$ with $\alpha \in (1, 2]$ for $i = 1, 2$. Then, $Z_1 + Z_2 \sim S(\alpha, \beta, \lambda, \mu)$ where $\beta = \frac{\beta_1\lambda_1^\alpha + \beta_2\lambda_2^\alpha}{\lambda_1^\alpha + \lambda_2^\alpha}$, $\lambda = (\lambda_1^\alpha + \lambda_2^\alpha)^{1/\alpha}$, $\mu = \mu_1 + \mu_2$.

Property 5: The pdf of a SαS variable, $Z \sim S(\alpha, 0, \lambda, 0)$ with $\alpha \in (1, 2]$ is defined as

$$p_Z(z) = \frac{1}{2\pi}\int_{-\infty}^{\infty} e^{-|\lambda t|^\alpha} e^{-jtz}dt. \quad (4)$$

III. UNIFIED MODELING FRAMEWORK

In this section, we provide an unified modeling framework and analyze the communication link shown in Fig. 1, in which the receiver antenna of the Lunar Gateway is directed to a transmitter antenna of the user on the lunar surface. First, we introduce the generalized system model with the relationship between the lunar surface temperature and the receiver noise temperature. Considering this relationship as well as other potential threats and anomalies, we then present the generalized channel model for cislunar communication.

A. GENERALIZED SYSTEM MODEL

The power of the received signal at the Lunar Gateway is calculated as follows according to the Friis equation, taking the line of sight into account.

$$P_r = P_t \frac{G_t G_r c^2}{(4\pi f d)^2 L_t L_r}, \quad (5)$$

where c is the speed of light, f is the frequency, d is the distance, L_t and L_r represent the losses due to transmitter and receiver equipment. P_r and P_t denote the power of the

received and transmitted signal. G_t and G_r are the antenna gain of the transmitter and receiver that is given as

$$G = \eta_A \left(\frac{D\pi f}{c} \right)^2, \qquad (6)$$

where D is the diameter of the antenna and η_A is the antenna aperture efficiency.

The power of the noise for per Hertz is calculated according to the Rayleigh–Jeans law [74], [75] as

$$N_0 = kT_{op}, \qquad (7)$$

where k is the Boltzmann constant ($\approx 1.38 \times 10^{-23} J/K$), and T_{op} is the operational equivalent noise temperature. T_{op} is calculated depending on cosmic microwave background noise temperature (T_{CMB}), antenna noise temperature (T_A), transmission line temperature (T_{TL}), and receiver noise temperature (T_R) as follows

$$T_{op} = T_{CMB} + T_A + \frac{1}{\eta_{rad}} T_{TL} + \frac{1}{\eta_{rad}\eta_{TL}} T_R, \qquad (8)$$

where η_{rad} and η_{TL} show the radiation efficiency and the thermal efficiency of the transmission line.

When the receiver antenna has losses, antenna noise temperature T_A counts external and internal noise temperatures in it. The external noise temperature of the antenna, $T_{A,external}$ is aroused from the brightness temperature[1] of the subtended body $T_B(\theta_A, \varphi_A)$ and calculated as [76], [77], [78]

$$T_{A,external} = \frac{1}{\Omega_A} \oiint_{4\pi} \overline{F}(\theta_A, \varphi_A) T_B(\theta_A, \varphi_A) d\Omega. \qquad (9)$$

Here, Ω_A is the antenna solid angle and $\overline{F}(\theta_A, \varphi_A)$ is the antenna normalized power pattern depending on the observation angles (θ, φ).

If there are no unexpected sources of radiation, it can be assumed that $T_B(\theta_A, \varphi_A) = T_B$, the brightness temperature is the same in all directions of antenna surrounding [77]. Then, the equation (9) is simplified and the increase in the external antenna noise temperature ($\Delta T_{A,external}$) is calculated as

$$\Delta T_{A,external} = \begin{cases} T_B, & \Omega_M \gg \Omega_A \\ \frac{\Omega_B}{\Omega_A} T_B, & \text{otherwise} \end{cases} \qquad (10)$$

where Ω_M and Ω_A represent the solid angles of the Moon and the antenna, respectively. However, the noise sources in radio astronomy show random polarization and this cause to receive half of power by the antenna. Therefore the correction factor is added as seen below [77].

$$\Delta T_{A,external} = \begin{cases} \frac{1}{2} T_B, & \Omega_M \gg \Omega_A \\ \frac{\Omega_M}{2\Omega_A} T_B, & \text{otherwise} \end{cases} \qquad (11)$$

Ω_A can be approximated in steradian depending on the half power beam width (HPBW) of the antenna in the planes of the observation angles as [77]

$$\Omega_A \simeq \theta_{A,HPBW} \varphi_{A,HPBW}. \qquad (12)$$

[1]The physical temperature results in the brightness temperature, depending on the radiation properties of the surface and the wavelength [50].

The solid angle subtended by Moon at the distance d_M for any $d_M \geq R_M$ is calculated in steradian as

$$\Omega_M = 2\pi \left(1 - \frac{\sqrt{d_M^2 - R_M^2}}{d_M^2} \right), \qquad (13)$$

where R_M is the radius of the Moon (≈ 1737 km). The internal antenna noise temperature, $T_{A,internal}$ is caused by the physical temperature of the antenna T_{AP} and calculated as

$$T_{A,internal} = T_{AP} \left(\frac{1}{\eta_{rad}} - 1 \right). \qquad (14)$$

Here, η_{rad} is radiation efficiency of the antenna. The transmission line noise temperature depends on the physical temperature of the transmission line (T_{TLP}) and is calculated as follows

$$T_{TL} = T_{TLP} \left(\frac{1}{\eta_{TL}} - 1 \right). \qquad (15)$$

As can be seen from the above equations, the noise signal is influenced by temperature fluctuations in the surrounding area of the transmitter to which the receiver antenna is directed. We can also heuristically notice that the noise shows impulsive characteristic, especially when the transmitter moves between sunlit and shadowed areas on the lunar surface.

B. GENERALIZED CHANNEL MODEL
The presence of non-Gaussian and Gaussian signals should be considered for the aspects of communication in cislunar space. Therefore, we utilize generalization capability of the SαS distribution for non-Gaussian and Gaussian processes [67] and define the ASαSN variable as

$$n = \sqrt{A_1} G_1 + j\sqrt{A_2} G_2. \qquad (16)$$

Here, A_1 and A_2 are i.i.d. alpha-stable distributed variables follow $S(\alpha/2, 1, [\cos(\pi\alpha/4)]^{2/\alpha}, 0)$. G_1 and G_2 are i.i.d. Gaussian random variables follow $\mathcal{N}(0, \sigma^2)$. As proven in the Appendix A, n follows $n \sim S(\alpha, 0, 2^{(\frac{1}{\alpha} - \frac{1}{2})}\sigma, 0)$. Note that for the special case of $\alpha = 2$, n can also be defined as a Gaussian variable and represented as $n \sim \mathcal{N}(0, 2\sigma^2)$ or $n \sim S(2, 0, \sigma, 0)$.

Proof: The proof is presented in Appendix A. ∎

The received signal at the cislunar spacecraft (Lunar Gateway) as follows

$$y = \sqrt{P_r} hx + n, \qquad (17)$$

where x represents the modulated symbol and h is the complex fading coefficient. We use Nakagami-m fading model, since it corresponds to the Rayleigh[2] fading but also can be approximated with Rician,[3] mild or no[4] fading cases [79].

[2]Nakagami-m fading model corresponds Rayleigh fading for $m = 1$.

[3]Nakagami-m fading model approximates Rician fading well for $m = (K + 1)^2/(2K + 1)$ where K is the Rician fading parameter.

[4]Nakagami-m fading model converges to non-fading when $m \to \infty$.

IV. THEORETICAL PERFORMANCE ANALYSIS

The ergodic capacity and outage probability are fundamental to the development of reliable communication. In this section, we investigate these metrics for the introduced channel model (in Section III-B), which allows a comprehensive analysis for both Gaussian and non-Gaussian processes under Nakagami-m fading. However, there is no exact capacity formulation for ASαSN channels when the noise stability is unknown or uncertain. Therefore, we use the lower bound of the capacity in [71], which also applies to the Shannon capacity under the Gaussian assumption $\alpha = 2$.

The capacity of the ASαSN channel with $\alpha \in (1, 2]$ is defined in [71] by solving the optimization problem below.

$$\max_{p(x) \in \mathcal{P}} I(X; Y)$$
$$\text{subject to } \mathbb{E}[|X|] \le P_c, \qquad (18)$$

where $\mathcal{P}$ denote the collection of Borel probability and $p(x)$ is all possible distributions for random input variables X. $I(X; Y)$ is the mutual information of the channel given by $Y = X + N$, where N and Y represent random noise and output variables, respectively. The input variables of the channel are subject to the constraint $P_c > 0$. The authors of [71] solve the optimization problem above and prove that (18) leads to the tractable lower bound of the capacity as follows

$$C \ge \frac{1}{\alpha} \log_2 \left(1 + \left(\frac{P_c}{\mathbb{E}[|N|]} \right)^\alpha \right). \qquad (19)$$

The study also shows analogy between the $\frac{P_c}{\mathbb{E}[|N|]}$ and SNR under Gaussian noise. We used the above boundary as the basic for our theoretical analyses.

As seen in Property 1, SαS variables for $\alpha < 2$ have no finite second-order moments, so the instantaneous received SNR under ASαSN is expressed by using the $\frac{P_c}{\mathbb{E}[|N|]}$ ratio as follows

$$\gamma = \left(\frac{P_c |h| \pi}{2 \lambda_n \Gamma \left(1 - \frac{1}{\alpha} \right)} \right)^\alpha. \qquad (20)$$

Lemma 1: Let $\bar{\gamma}$ be the average SNR and let $\xi = \mathbb{E}[|h|^\alpha]$ be the expected value of $|h|^\alpha$. Then, the pdf of the instantaneous received SNR for Nakagami-m fading channel under ASαSN, $f(\gamma)$ is derived as

$$f_\gamma(\gamma) = \frac{2 m^m \gamma^{-1}}{\Omega \alpha \Gamma(m)} \exp\left[-\frac{m}{\Omega} \left(\frac{\gamma \xi}{\bar{\gamma}} \right)^{\frac{2}{\alpha}} \right] \left(\frac{\gamma \xi}{\bar{\gamma}} \right)^{\frac{2m}{\alpha}}, \quad (21)$$

where m denotes the Nakagami-m fading parameter and Ω is the mean-square of the fading amplitude.

Proof: The proof is presented in Appendix B. ∎

A. LOWER BOUNDS OF ERGODIC CAPACITY

Wireless communication channels often encounter different propagation conditions, which makes the development of communication systems to adapt the transmission rate to the instantaneous channel capacity a challenge. Therefore,

communication systems are designed to operate at ergodic capacity to ensure a sustainable information rate, in other words reliable communication.

The ergodic capacity is statistical average of the mutual information depending on the fading and receiver side information [80]. Then, the lower bound of the ergodic capacity for the ASαSN channel is written by substituting (19) as follows

$$\overline{C} \ge \mathbb{E} \left[\frac{1}{\alpha} \log_2(1 + \gamma) \right]$$
$$\ge \frac{1}{\alpha} \int \log_2(1 + \gamma) f(\gamma) d\gamma. \qquad (22)$$

Theorem 1: The ergodic capacity for a Nakagami-m fading channel under ASαSN is lower bounded by using Lemma 1 as follows

$$\overline{C} \ge \frac{\Omega^{m-1} l}{2 \ln(2) \Gamma(m)} \sqrt{\frac{k^{2m-3}}{(2\pi)^{2l+k-3}}} \qquad (23)$$
$$\times G_{2l,k+2l}^{k+2l,l} \left[\frac{(\xi/\bar{\gamma})^l}{(k \Omega m^{-1})^k} \middle| \begin{array}{l} I(l, 0), I(l, 1) \\ I(k, m), I(l, 0), I(l, 0) \end{array} \right].$$

Here, $I(\rho, \iota) \triangleq \iota/\rho, (\iota+1)/\rho, \ldots, (\iota + \rho - 1)/\rho$ with ι an arbitrary real value, and $\frac{l}{k} = \frac{2}{\alpha}$ while $\rho, k, l \in \mathbb{Z}^+$.

Proof: The proof is presented in Appendix C. ∎

B. UPPER BOUNDS OF OUTAGE PROBABILITY

The ergodic capacity provides important insights for the development of reliable communication, but does not guarantee the continuity of the desired transmission rates. There may be poorer channel conditions or unexpected anomalies, which is quite possible in cislunar space, and so communication may occasionally be interrupted. Furthermore, this can cause a critical problem for core systems that use real-time control applications during cislunar missions.

The outage probability indicates the likelihood of communication failures and is analyzed to reduce the risk for robust and reliable communication. When the desired data rate is achieved with an instantaneous received SNR of greater than or equal to γ_{th}, the outage probability is upper bounded as follows

$$P_{\text{out}}(\gamma_{th}) \le \int_0^{\gamma_{th}} p_\gamma(\gamma) d\gamma. \qquad (24)$$

Theorem 2: The outage probability for Nakagami-m fading channel under ASαSN is upper bounded by using Lemma 1 as

$$P_{\text{out}}(\gamma) \le \frac{\Omega^{m-1}}{\Gamma(m)} \left[\Gamma(m) - \Gamma \left(m, \frac{(\gamma \xi/\bar{\gamma})^{\frac{2}{\alpha}}}{\Omega m^{-1}} \right) \right]. \qquad (25)$$

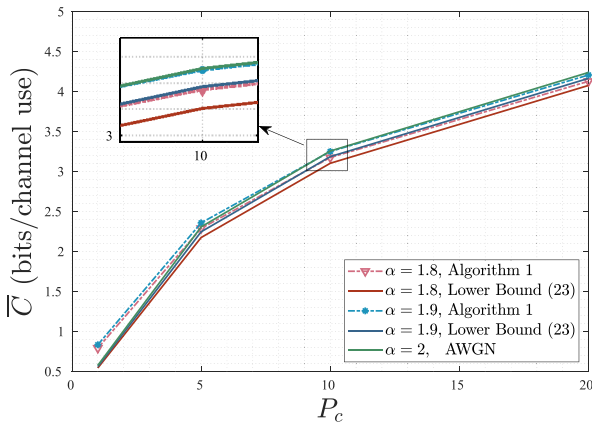*Proof:* The proof is presented in Appendix D. ∎

FIGURE 2. Comparisons of the closed-form lower bound for ergodic capacity in equation (23) and numeric capacity approximation algorithm with $m = 1$ and $\alpha \in \{1.8, 1.9, 2\}$.

FIGURE 3. Comparisons of the closed-form lower bound for ergodic capacity in equation (23) and numeric capacity approximation algorithm with $m = 5$ and $\alpha \in \{1.8, 1.9, 2\}$.

FIGURE 4. Comparisons of the closed-form lower bound for ergodic capacity in equation (23) and numeric capacity approximation algorithm with $m = 15$ and $\alpha \in \{1.8, 1.9, 2\}$.
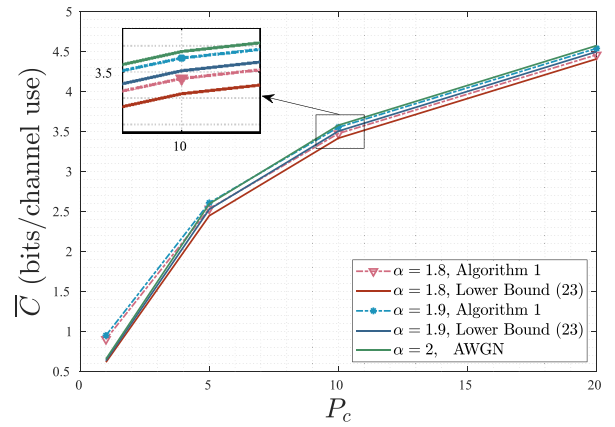
C. NUMERICAL APPROXIMATION FOR ERGODIC CAPACITY

The theoretical bounds for the ergodic capacity are presented in closed-form under ASαSN and Nakagami-m fading. Since we perform the derivations with closed-form expressions, the bound in Theorem 2 preserves the tightness of the basic bound in equation (19). However, in this section, we propose to show the tightness of the bound to give a clear insight into our results in the following section. We compare the lower bound of the ergodic capacity with the numerically approximated capacity values using the Blahut-Arimoto algorithm for the ASαSN in [71].

The Blahut-Arimoto algorithm is a well-known capacity approximation algorithm for discrete memoryless channels where the inputs must be discrete and with a finite alphabet. To the best of our knowledge, this is the first in the literature where the Blahut-Arimoto algorithm has been adapted for the presence of fading, as detailed in Algorithm 1. We defined the channel as follows

$$Y = h_i X + N, \quad i = 1, 2, \ldots, N_h, \tag{26}$$

where h_i is a fading coefficient, X and N are random variables with finite alphabets S_X and S_N with lengths M_X and M_N, respectively. In Algorithm 1, we compute the capacity values for each h_i and then obtained the approximation to the ergodic capacity using Riemann summation [81] in step (5). The rest of the algorithm is implemented in the same way as in [71].

Figures 2, 3 and 4 demonstrate the tightness of the closed-form lower bound in equation (23) for three fading and stability conditions individually while channel inputs are subject to the constraint $P_c \in \{1, 5, 10, 20\}$. The results also include the ergodic capacity for AWGN channel that can also be considered ASαSN channel with $\alpha = 2$. All results are obtained by setting the shift parameter of noise variables $\lambda = 1/\sqrt{2}$ that is identical with unit variance for noise variables in AWGN channel as proven in Appendix A.
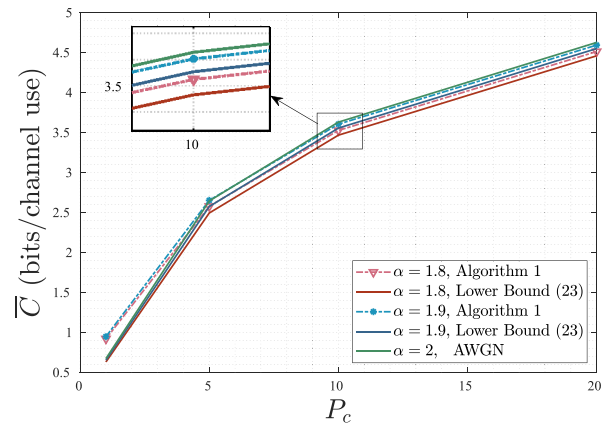
We compare the lower bound and numerical approximation of ergodic capacity in Fig. 2 for Nakagami-m fading parameter $m = 1$ that corresponds to Rayleigh fading or Rician fading with $K = 0$. Fig. 2 indicates the impact of α values on the ergodic capacity and the compatibility of the lower bound in equation (23). For example, under the constraint of $P_c = 5$, the approximate results of the ergodic capacity are 2.2883 bits per channel use (bpcu) and 2.3573 bpcu for $\alpha = 1.8$ and $\alpha = 1.9$, respectively while the ergodic capacity is 2.3066 bpcu for $\alpha = 2$.

Fig. 3 shows the results for better fading condition with $m = 5$, which can also be considered for Rician fading with $K \approx 8.5$. In Fig. 3, we observe that the lower bound are packed with the approximate average capacity tightly and how the ergodic capacity increases with improved propagation and noise conditions.

The same comparison is presented in Fig. 4 to show the results for mild fading with Nakagami-m fading parameter $m = 15$. The closeness between the closed-form lower bound and the numerical approximation for capacity does not alter

depending on m parameter. In the zoomed window, for $\alpha = 1.9$ and $P_c = 10$, the numerical approximation of the ergodic capacity by Algorithm 1 is 3.6028 bpcu, while the theoretical bound by (23) is 3.5536 bpcu. For $\alpha = 1.8$ and $P_c = 10$, these results are 3.5242 and 3.4652 bpcu, respectively. The differences between the numerical approximation and the bound are 0.0492 and 0.059 for $\alpha = 1.9$ and $\alpha = 1.8$, respectively. We observe that the tightness of the bound decreases slightly with decreasing alpha values, just as with the basic bound in [71]. Overall, the results show that the lower bound for ergodic capacity is tighter in the case $\alpha = 1.9$ compare to $\alpha = 1.8$ exactly like to the behavior[5] of the basic bound in (19). This also shows that closed-form expressions in Section IV do not affect the tightness of (19) but also the performance of Algorithm 1.

V. PERFORMANCE ANALYSIS AT SYSTEM LEVEL
A. CSN ARCHITECTURE: LUNAR GATEWAY
We propose the cislunar communication through the communication link of Lunar Gateway, as shown in Fig. 1. It is orbiting in NRHO, unlike others, and is a far preferable relay orbiter as its presence is projected at least 15 years [13]. Another key factor in the popularity of Lunar Gateway is its design, which aims to provide broader dynamic connectivity with maximum interoperability [14]. It is capable of providing both low and high data rate mission services for users on the lunar surface or in orbit. Thanks to its eligibility for mission objectives, Lunar Gateway designed to support not only the most critical Artemis missions, many lunar missions including commercial payload services and inter-agency purposes, but also future deep space missions [12], [13], [14]. Therefore, it is also seen as an important attempt to determine the future standards of CSNs.

For the communication scenario considered in this study, as shown in Fig. 1, Lunar Gateway is the receiver and the transmitter is a rover on the lunar surface, which is also the communication terminal of the mission. The communication terminal transmits the communication signals over S band (2200 - 2290 MHz) or Ka band (27 - 27.5 GHz) [14]. The targeted maximum data rates for the link from lunar rover to the Lunar Gateway are 4 Msps and 100 Mbps in S and Ka bands [83], respectively. In accordance with the mission objectives and the use case of bands, we determine the bandwidths for each band, as shown in Table 1.

B. SIMULATION SET-UP AND CONFIGURATION
All theoretical and system analyses are performed through intertwined results using the parameters in Table 1. By diversifying the worse and better conditions for different mission objectives, we aim to provide a broader insight into the development and optimization of robust cislunar

---

[5]Reference [71] shows that the tightness of (19) decreases on average by 1 bit for $\alpha = 1.1$ and that it is consistent with our results for $\alpha = 1.9$. Note that we do not consider the highly extreme cases in this study that disrupt the channel stability this level.

TABLE 1. Link budget parameters for the communication links [13], [14], [82], [83], as shown in Fig. 1.

Parameters		Unit	Lunar Surface to Lunar Gateway	
			S Band	**Ka Band**
f		MHz	2245	27250
Bandwidth		MHz	1	10
Transmitter	P_t	W	1, 10	
	$\eta_{A,t}$	%	43	
	D_t	m	0.254	
	G_t	dBi	11.85	28.27
	L_t	dB	1	
Receiver	$\eta_{A,r}$	%	54	
	D_r	m	1.5	
	G_r	dBi	33.53	49.95
	L_r	dB	3	
	T_{AP}	K	300	
	T_R	K	50	
	T_{TLP}	K	300	
	η_{rad}	%	95	
	η_{TL}	%	99	
T_{CMB}		K	2.725	

communication. Before we present the results for the ergodic capacity and the outage probability, we explain for the system set-up and configurations below.

- The brightness temperature of Moon changes daily as the Moon, Earth and sun orbit each other. As the Lunar Gateway's antenna is pointed at the transmitter on the lunar surface, the noise temperature of the receiver changes depending on T_B. Our results cover the range of T_B from 0 to 600 K.
- While the Lunar Gateway is moving in NRHO and pointing the antenna at a lunar rover, the lunar rover is also moving between sunlit and shadowed areas. As a result of these and other uncertainties, the noise temperature (so the communication signals) can show an impulsive behavior. With this in mind, we extend the results for three different conditions of noise stability with $\alpha \in \{1.8, 1.9, 2\}$.
- During the missions, the propagation mechanisms vary due to the arrival angles of the signal or multifaceted and dynamic nature of the lunar surface. Our results include three fading conditions with $m \in \{1, 5, 15\}$.
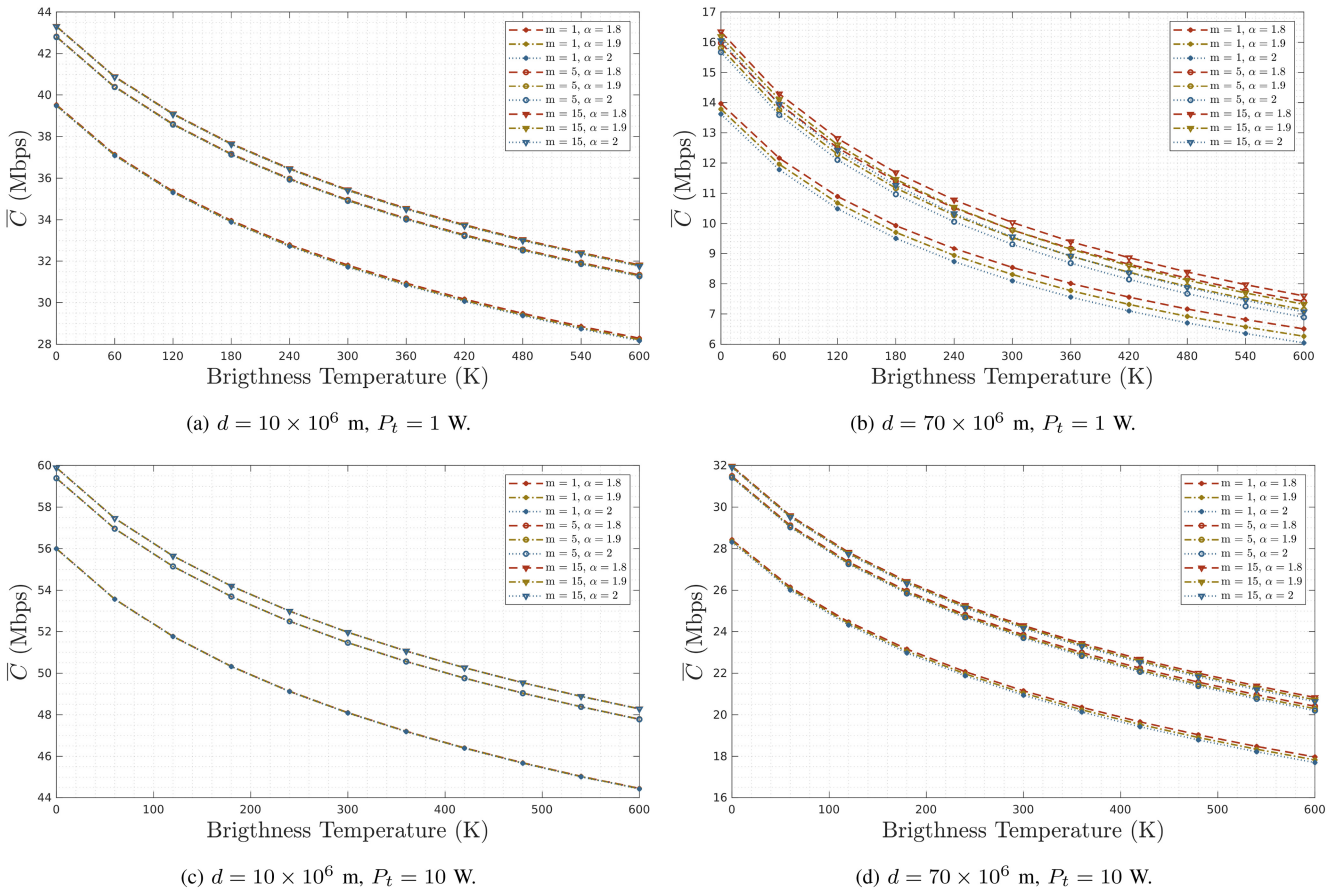
(a) $d = 10 \times 10^6$ m, $P_t = 1$ W.

(b) $d = 70 \times 10^6$ m, $P_t = 1$ W.

(c) $d = 10 \times 10^6$ m, $P_t = 10$ W.

(d) $d = 70 \times 10^6$ m, $P_t = 10$ W.

FIGURE 5. The comparison of the ergodic capacity with the lower bound in equation (23) depending on the brightness temperature and under different system settings for the Ka band.

- The results are extended for the S and Ka band, taking into account mission targets with low and high data rates. The simulations are performed for center frequency of each band [13].
- Due to the orbital motion of the Lunar Gateway, the distance (d) between the transmitter and receiver changes considerably and thus also the path loss and the SNR. Therefore, the results are presented for minimum (10×10^6 m) and maximum (70×10^6 m) distances to observe edge cases.
- By considering power constraints, we analyze the communication link for two transmit power $P_t \in \{1, 10\}$.

C. ERGODIC CAPACITY LOWER BOUND

The results for the lower bound of the ergodic capacity are presented separately for each band in this section. As mentioned, the system settings are varied to investigate the susceptibility of cislunar communication and to gain insights into the design and development of future CSNs.

Fig. 5 shows the relationship between the brightness temperature and the lower bound of the ergodic capacity for Ka band under different combinations of system and channel parameters, such as the distance between the transmitter (Tx)

and receiver (Rx), the transmit power, the noise stability index (α-values) and the fading conditions. The lower bound of the ergodic capacity varies considerably and ranges from 6 Mbps to 60 Mbps.

Fig. 5(a) presents the results for the minimum Tx-Rx distance and the lowest transmit power. The lower bound of the ergodic capacity decreases significantly from 43.5 Mbps to 28 Mbps when the brightness temperature increases from 0 K to 600 K. However, changes in noise stability (α-values) have no significant influence on the ergodic capacity. Instead, it is the fading conditions that cause differences in the ergodic capacity, about 15.5 Mbps, when the brightness temperature increases. At the maximum Tx-Rx distance with the lowest P_t, as shown in Fig. 5(b), the ergodic capacity decreases further, from 6 Mbps to 16.5 Mbps, which is due to the increased path loss associated with the longer distance. The effect of α-values becomes more pronounced compared to the results in Fig. 5(a), but worse noise conditions with lower α-values do not lead to a decrease in average capacity. This is because the α-values are kept constant, while the noise power changes with the brightness temperature. Consequently, the effect of increasing T_B is reflected in the noise scale parameter more than the noise stability index, leading to $\lambda_{\alpha=2} > \lambda_{\alpha=1.9} > \lambda_{\alpha=1.8}$. In other words,
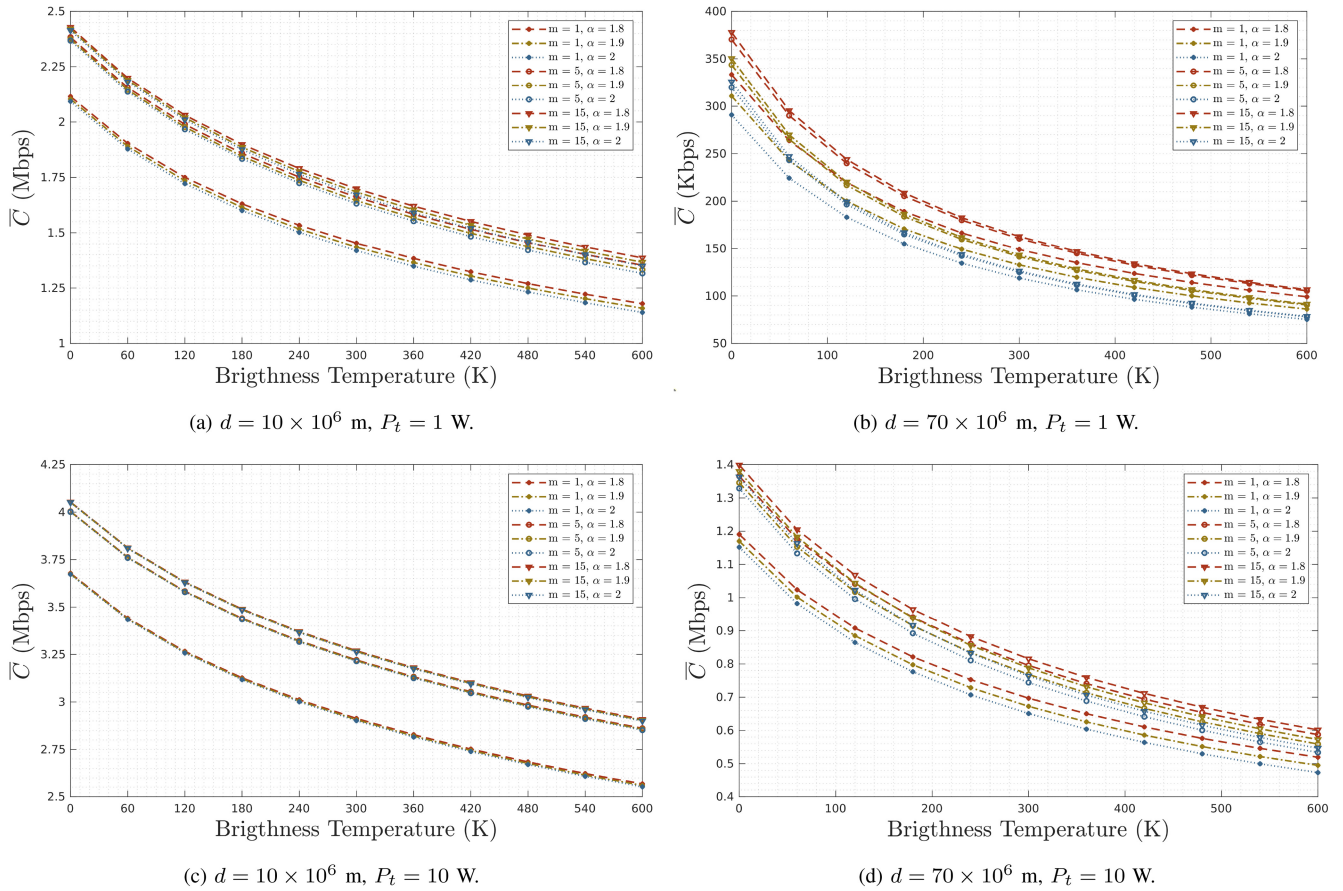
(a) $d = 10 \times 10^6$ m, $P_t = 1$ W.

(b) $d = 70 \times 10^6$ m, $P_t = 1$ W.

(c) $d = 10 \times 10^6$ m, $P_t = 10$ W.

(d) $d = 70 \times 10^6$ m, $P_t = 10$ W.

FIGURE 6. The comparison of the ergodic capacity with the lower bound in equation (23) depending on the brightness temperature and under different system settings for the S band.

the ergodic capacity becomes more sensitive to brightness temperature at a high noise stability index, as it leads to larger changes in λ-values. *Increasing bandwidth is an effective way to reduce the impact of λ-values on ergodic capacity, but this may not be possible due to bandwidth constraints. Therefore, an accurate estimation of the λ-value is a mandatory requirement for the design of communication systems. But the estimation of the α-value must also be correct, as it is a prerequisite for the accurate estimation of the λ-value. In this way, we ensure that the noise scale parameter and thus the average capacity performance are maintained at a lower sensitivity.*

Figs. 5(c) and 5(d) present the results at the highest P_t for the minimum and maximum Tx-Rx distances, respectively. The effect of brightness temperature and fading conditions remains significant and leads to decreases in ergodic capacity from 60 Mbps to 44.5 Mbps, as shown in Fig. 5(c), and from 32 Mbps to 17.5 Mbps, as shown in Fig. 5(d). However, increasing P_t raises the ergodic capacity by about 16 Mbps under all conditions in Fig. 5(c) compared to Fig. 5(a). A similar improvement is observed between Fig. 5(d) and Fig. 5(b). *This indicates that increasing the transmit power is an effective way to mitigate the effects of the λ-value and distance while achieving more stable performance.*

Fig. 6 illustrates the relationship between the brightness temperature and the lower bound of the ergodic capacity for different system configurations in the S band. The results show that the ergodic capacity ranges between 70 Kbps and 4.1 Mbps, depending on the system and channel parameters. Fig. 6(a) shows the results for the minimum Tx-Rx distance and the lowest transmit power. The increase in brightness temperature and the deteriorating fading conditions lead to a decrease in the ergodic capacity from 2.45 Mbps to 1.15 Mbps. In fact, communication signals in S band are less vulnerable to noise fluctuations than the Ka band due to its longer wavelength and thus the higher P_r. However, unlike the results shown in Fig. 5(a) for the Ka band, the effect of noise stability on the ergodic capacity is clearly visible due to the small range of the y-axis. *This also suggests that accurate estimation of the λ and α values in S band is essential to ensure lower susceptibility to performance degradation in average capacity.*

Fig. 6(b) shows the results for the maximum distance with the lowest P_t. Since the distance between the Lunar Gateway and the Moon is the greatest, the lower bounds of the ergodic capacity fall in the range of 70 to 380 Kbps. It also clearly shows how the α-values together with the brightness temperature affect the ergodic capacity. The gap between
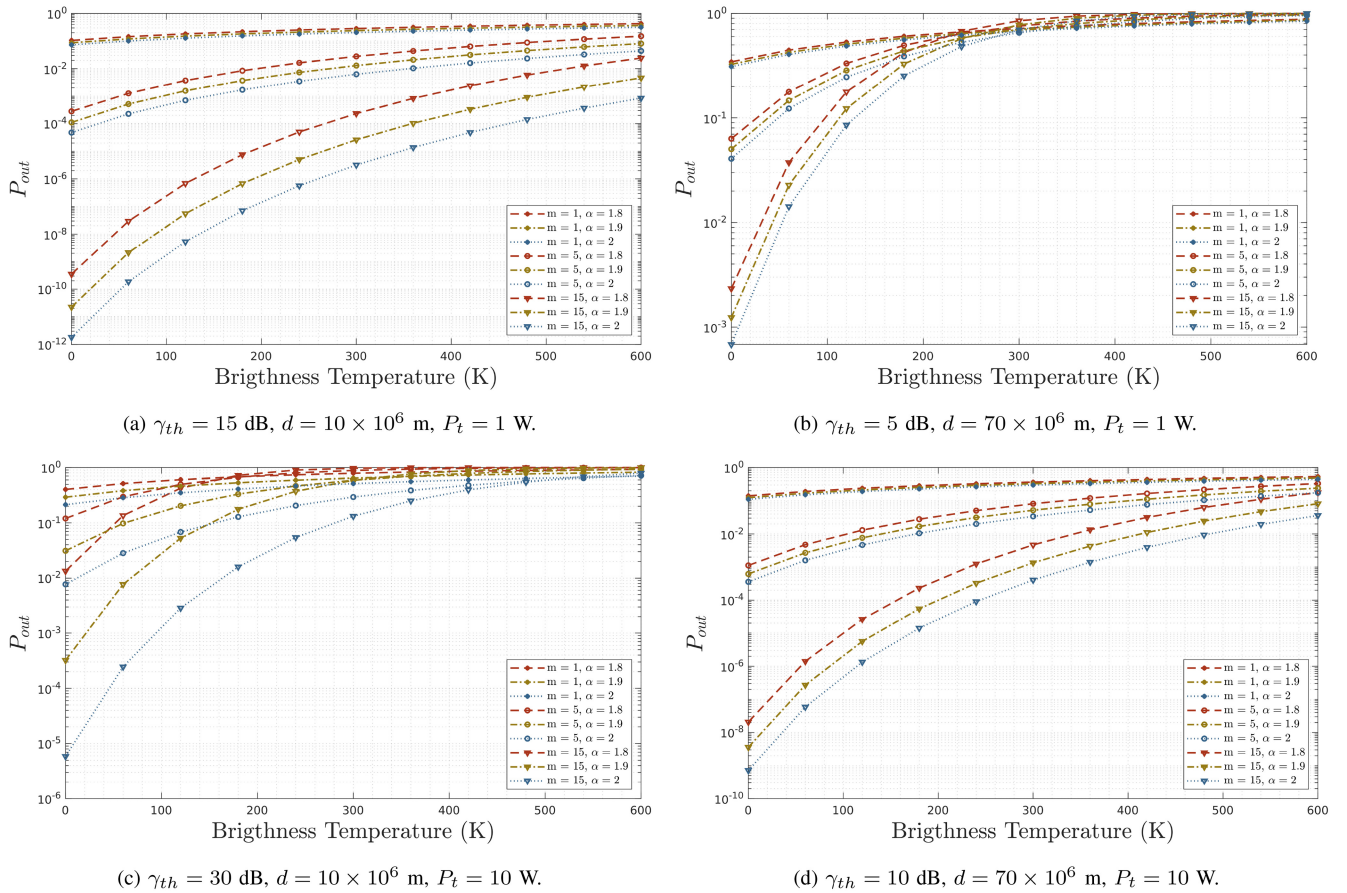
(a) $\gamma_{th} = 15$ dB, $d = 10 \times 10^6$ m, $P_t = 1$ W.

(b) $\gamma_{th} = 5$ dB, $d = 70 \times 10^6$ m, $P_t = 1$ W.

(c) $\gamma_{th} = 30$ dB, $d = 10 \times 10^6$ m, $P_t = 10$ W.

(d) $\gamma_{th} = 10$ dB, $d = 70 \times 10^6$ m, $P_t = 10$ W.

FIGURE 7. The comparison of the outage probability with the upper bound in equation (25) depending on the brightness temperature and under different system settings for the Ka band.

the worst fading conditions significantly narrows compared to the other results in Figs. 5 and 6. Similar to Fig. 5, we observe that capacity is higher in all parameter settings in Fig. 6(c), which presents the results for the minimum Tx-Rx distance with the highest P_t. The average capacity decreases from 4.05 Mbps to 2.6 Mbps with increasing brightness temperature and worse fading conditions. At the maximum Tx-Rx distance and the highest P_t, as shown in Fig. 6(d), the lower bounds of the ergodic capacity fall in the range of 0.4 Mbps to 1.4 Mbps due to larger path loss caused by the longer distance. Despite the increase in P_t, the influence of the noise parameters remains evident in Fig. 6(d), as it is in Figs. 6(a) and 6(b).

D. OUTAGE PROBABILITY UPPER BOUND
In the previous section, we presented the results for ergodic capacity under different system configurations. In particular, we observed how the noise scale parameter varies significantly while the noise stability index remains constant due to the brightness temperature. We have addressed how the ergodic capacity becomes more vulnerable depending on the noise scale parameter if the α-value is not accurately estimated. In this section, we propose to focus on the instantaneous capacity performance over the outage probability.

This approach allows us to directly observe the impact of the α-value on the capacity. The results based on equation (25) are presented separately for Ka and S bands, along with comprehensive analyses in Figs. 7 and 8.

Fig. 7(a) illustrates the outage probability at the minimum Tx-Rx distance and lowest transmit power. The differences in the outage probabilities under different fading conditions can be clearly seen. Notably, the outage probability for $m = 1$, which corresponds to Rayleigh fading, is intolerable for reliable cislunar communication. As expected, the outage probability increases together with brightness temperature even under more favorable fading conditions. More importantly, the figure shows how variations in α-values can lead to unexpected communication interruptions for the Ka band. For example, P_{out} at $T_B = 120$ K and $m = 15$ is less than 10^{-8} for $\alpha = 2$, but it increases to about 10^{-6} for $\alpha = 1.8$.

As the distance between transmitter and receiver reaches its maximum at the lowest P_t, P_{out} increases significantly, as can be seen in Fig. 7(b). Although the threshold value for the instantaneous SNR is lowered by 10 dB compared to Fig. 7(a), the outage probabilities are unacceptable at brightness temperatures greater than 100 K, even in the case of $m = 15$. This is especially a critical problem for real-time control applications of CSNs and missions. Fig. 7(b) also
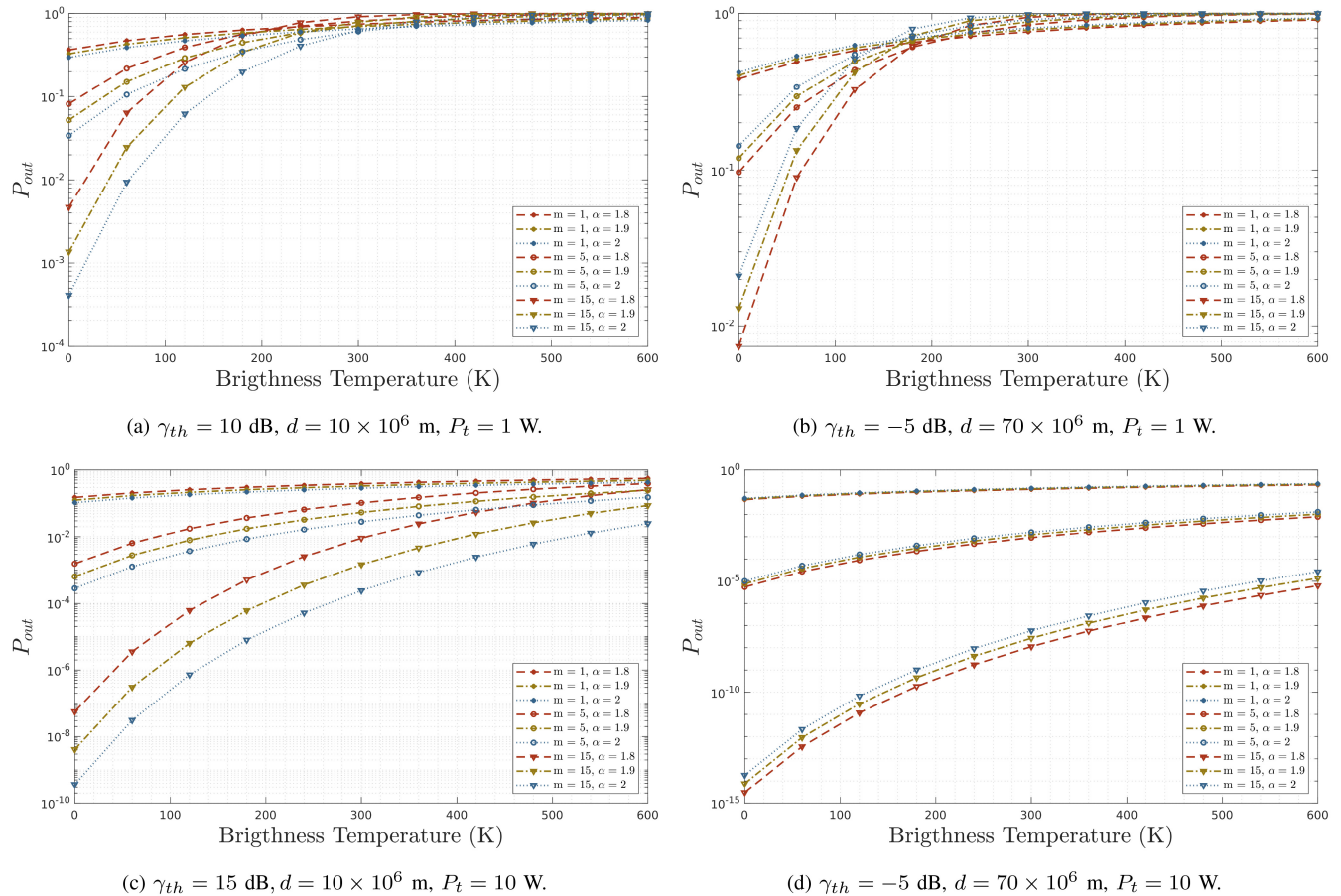
(a) $\gamma_{th} = 10$ dB, $d = 10 \times 10^6$ m, $P_t = 1$ W.

(b) $\gamma_{th} = -5$ dB, $d = 70 \times 10^6$ m, $P_t = 1$ W.

(c) $\gamma_{th} = 15$ dB, $d = 10 \times 10^6$ m, $P_t = 10$ W.

(d) $\gamma_{th} = -5$ dB, $d = 70 \times 10^6$ m, $P_t = 10$ W.

FIGURE 8. The comparison of the outage probability with the upper bound in equation (25) depending on the brightness temperature and under different system settings for the S band.

illustrates the joint influence of the propagation and noise stability conditions as well as the brightness temperature. However, it also shows that the considerations outlined in this article are crucial to ensure reliable and dynamic CSNs.

Fig. 7(c) compares the P_{out} at the minimum distance and the highest transmit power. The effect of the noise stability index becomes clearer compared to the other figures when the threshold value for the instantaneous SNR – i.e., the target data rate – is increased. This shows that the impulsiveness of the communication signal leads to more communication interruptions for missions requiring high data rates. *It also sheds light on the trade-offs between mission design and objectives. For example, a mission operating in a more challenging propagation environment may require a power system that ensures communication at a higher transmit power, or alternatively be designed with a lower data rate objective.* Fig. 7(d) shows the results at the maximum distance and highest P_t. Decreasing the threshold for the received instantaneous SNR does not prevent the increase in the outage probability, which is primarily caused by the increasing path loss. *This suggest that higher transmit power is required to maintain reliable cislunar communication,* *especially at increasing Tx-Rx distance and under worse fading conditions.*

Fig. 8 compares the outage probabilities for the S band in accordance with the system set-up and configurations in Section V-B. Fig. 8(a) shows the results at minimum distance and lowest transmit power. The results are acceptable except for the worst fading conditions. However, the risk for communication failures is generally unacceptable in Fig. 8(b), which presents the results at the maximum distance and the lowest transmit power. The outage probability is more sensitive to the noise scale parameter than to the noise stability index as the brightness temperature increases, similar to the results observed for the ergodic capacity. However, this effect is not seen in Fig. 7(b), which shows the results for the same system configurations in Ka band. The reason for this difference is that the S band has a larger wavelength, resulting in lower received power under the same system conditions. *This indicates that possible solutions to improve P_r should be considered when developing communication systems, such as reducing system losses or increasing transmit power.*

Fig. 8(a) presents the results for the P_{out} at the minimum distance and the lowest P_t for an instantaneous SNR

threshold of 15 dB. We observe that the performance, especially for $m = 15$, improves for all values of the noise stability index and allows higher data rate targets. In contrast, for $m = 1$, either the target data rates – γ_{th} in other words – should be reduced or the transmit power should be increased to ensure reliable communication. Fig. 8(d) shows the P_{out} at maximum distance and highest P_t. If we compare the results in Figs. 8(a) and 8(d), increasing the transmit power improves the outage probability significantly. However, the instantaneous capacity remains very sensitive to the values for α and λ, as in Fig. 8(b), due to the lower received power.

Overall, the results illustrate the significant influence of brightness temperature and variations in noise properties, but also show the importance of their accurate estimation. Furthermore, the effects of distances due to cislunar geometry, changing propagation and noise conditions, and power and bandwidth constraints become clear with the results. In this way, they highlight the trade-offs between designs, objectives and system constraints of missions through the extensive system and channel settings. These results can also serve as inspiration for further studies focusing on deep space communications, as Lunar Gateway is also intended to support deep space missions. However, deep space missions are likely to be more challenging in many aspects, as existing knowledge is still limited compared to cislunar space.

VI. CONCLUSION AND FURTHER WORK
With respect to the emerging CSNs with outstanding goals, we propose system-level and theoretical analyses for cislunar communication to give an outlook on their dynamic and robust designs in the future. Therefore, we first discussed the aspects of communication in cislunar space and the corresponding considerations, such as temperature fluctuation, hilly terrain with sunlit and shadowed areas, and high mobility. To analyze the reliable communication, we proposed the ergodic capacity and outage probability. Prior to our theoretical analyses, we investigated the relationship between the temperature variations on the lunar surface and the Lunar Gateway receiver. Since this relationship and other aspects of cislunar communication can lead to impulsivity and different propagations of communication signals, we introduced a signal model that takes these aspects into account. Then, we performed our theoretical analyses. Furthermore, in our results, we extend the analyses for both high and low data rate mission targets with comprehensive system configurations. The results clearly show the significant influence of many phenomena on the ergodic capacity and outage probability, but also to provide insights into the future communication systems of CSNs. For further studies, we plan to extend the design considerations in light of our current analysis to further develop CSNs.

APPENDIX A
Let define $n = n_1 + jn_2$ where $n_i = \sqrt{A_i}G_i$ for $i = 1, 2$. Here, $A_i \sim S(\alpha/2, 1, [\cos(\pi\alpha/4)]^{2/\alpha}, 0)$ and $G_i \sim \mathcal{N}(0, \sigma^2)$. Since the alpha-stable distribution is Gaussian when $\alpha = 2$

and $\beta = 0$, $G_i \sim S(2, 0, \frac{\sigma}{\sqrt{2}}, 0)$ is defined as well. Then, the characteristic function of n_i is written as

$$\begin{aligned} \Phi_{n_i}(t) &= \mathbb{E}\big[\exp(jtn_i)\big] \\ &= \mathbb{E}\Big[\exp\big(jtA_i^{1/2}G_i\big)\Big] \\ &= \mathbb{E}\Big[\mathbb{E}\Big[\exp\Big(-j|t|^2\Big(\tfrac{\sigma}{\sqrt{2}}\Big)^2 A_i\Big)\Big]\Big|A_i\Big]. \end{aligned} \tag{29}$$

By substituting the Laplace transform of A_i, $\mathbb{E}[\exp(-sA_i)] = \exp(-s^{(\alpha/2)})$

$$\Phi_{n_i}(t) = \mathbb{E}\Big[\exp\Big(-j|t|^\alpha\Big(\tfrac{\sigma}{\sqrt{2}}\Big)^\alpha\Big)\Big]. \tag{30}$$

We show that $n_i \sim S(\alpha, 0, \frac{\sigma}{\sqrt{2}}, 0)$, n is the sum of two $S\alpha S$ variables in other words. Then, it can be seen that $n \sim S(\alpha, 0, 2^{(\frac{1}{\alpha} - \frac{1}{2})}\sigma, 0)$ from Property 4.

APPENDIX B
Let $Y = |h|^\alpha$ and the cdf of Y is calculated as

$$\begin{aligned} F_Y(y) &= P\big(|h|^\alpha \le y\big) \\ &= P\big(|h| \le y^{1/\alpha}\big) \\ &= F_{|h|}\big(y^{1/\alpha}\big). \end{aligned} \tag{31}$$

By using above substitution, the pdf of $|h|^\alpha$ is derived as

$$\begin{aligned} f_{|h|^\alpha}(y) &= \frac{\partial F_{|h|}\big(y^{1/\alpha}\big)}{\partial y} \\ &= \frac{1}{\alpha}f_{|h|}\big(y^{1/\alpha}\big)y^{\frac{1}{\alpha}-1} \end{aligned} \tag{32}$$

$f_{|h|^\alpha}(y)$ is obtained by inserting the pdf of Nakagami-m distribution as follows

$$f_{|h|^\alpha}(y) = \frac{2m^m y^{-1}}{\Omega\alpha\Gamma(m)}\exp\Big[-\frac{m}{\Omega}y^{\frac{2}{\alpha}}\Big]y^{\frac{2m}{\alpha}}. \tag{33}$$

By employing a change of variable $|h|^\alpha = \frac{\gamma\xi}{\bar{\gamma}}$ within the cdf function of the instantaneous SNR, we derived the cdf of instantaneous SNR as a function of $F_{|h|^\alpha}(y)$ below.

$$\begin{aligned} F_\gamma(\gamma) &= P\Big(|h|^\alpha\frac{\bar{\gamma}}{\xi} \le \gamma\Big) \\ &= P\Big(|h|^\alpha \le \gamma\frac{\xi}{\bar{\gamma}}\Big) \\ &= F_{|h|^\alpha}\Big(\gamma\frac{\xi}{\bar{\gamma}}\Big) \end{aligned} \tag{34}$$

Using equation (34), $f_\gamma(\gamma)$ is derived as follows

$$\begin{aligned} f_\gamma(\gamma) &= \frac{\xi}{\bar{\gamma}}f_{|h|^\alpha}\Big(\gamma\frac{\xi}{\bar{\gamma}}\Big) \\ &= \frac{2m^m\gamma^{-1}}{\Omega\alpha\Gamma(m)}\exp\Big[-\frac{m}{\Omega}\Big(\frac{\gamma\xi}{\bar{\gamma}}\Big)^{\frac{2}{\alpha}}\Big]\Big(\frac{\gamma\xi}{\bar{\gamma}}\Big)^{\frac{2m}{\alpha}}. \end{aligned} \tag{35}$$

APPENDIX C

The average capacity for a Nakagami fading channel is lower bounded by substituting (21) into (22) as follows

$$\overline{C} \geq \int_0^\infty \frac{2m^m \gamma^{-1}}{\Omega \alpha \Gamma(m)} \log_2(1+\gamma)$$
$$\times \exp\left[-\frac{m}{\Omega}\left(\frac{\gamma\xi}{\bar{\gamma}}\right)^{\frac{2}{\alpha}}\right]\left(\frac{\gamma\xi}{\bar{\gamma}}\right)^{\frac{2m}{\alpha}} d\gamma \qquad (36)$$

The above integration is manipulated by utilizing substitutions in equations (37) and (38).

$$G_{2,2}^{1,2}\left[\gamma \left|\begin{matrix}1,1\\1,0\end{matrix}\right.\right] = \ln(1+\gamma). \qquad (37)$$

$$G_{0,1}^{1,0}\left[\frac{(\gamma\xi/\bar{\gamma})^{\frac{2}{\alpha}}}{\Omega m^{-1}}\left|\begin{matrix}-\\m\end{matrix}\right.\right] = \frac{(\gamma\xi/\bar{\gamma})^{\frac{2m}{\alpha}}}{\Omega^m m^{-m}}\exp\left[-\frac{(\gamma\xi/\bar{\gamma})^{\frac{2}{\alpha}}}{\Omega m^{-1}}\right]. \qquad (38)$$

Then, the equation (36) becomes as

$$\overline{C} \geq \frac{2\Omega^{m-1}}{\alpha^2 \ln(2)\Gamma(m)}$$
$$\times \int_0^\infty \gamma^{-1} G_{0,1}^{1,0}\left[\frac{(\gamma\xi/\bar{\gamma})^{\frac{2}{\alpha}}}{\Omega m^{-1}}\left|\begin{matrix}-\\m\end{matrix}\right.\right] G_{2,2}^{1,2}\left[\gamma\left|\begin{matrix}1,1\\1,0\end{matrix}\right.\right] d\gamma. \qquad (39)$$

The above integration is solved with the help of the equation in [84], [85] and the lower bound of the ergodic capacity for a Nakagami fading channel is derived as

$$\overline{C} \geq \frac{\Omega^{m-1} l}{2\ln(2)\Gamma(m)}\sqrt{\frac{k^{2m-3}}{(2\pi)^{2l+k-3}}}$$
$$\times G_{2l,k+2l}^{k+2l,l}\left[\frac{(\xi/\bar{\gamma})^l}{(k\Omega m^{-1})^k}\left|\begin{matrix}I(l,0),I(l,1)\\I(k,m),I(l,0),I(l,0)\end{matrix}\right.\right]. \qquad (40)$$

APPENDIX D

The upper bound of the outage probability is calculated by utilizing the equations (21) and (24) as

$$P_{\text{out}}(\gamma) \leq \int \frac{2m^m \xi}{\Omega \alpha \Gamma(m)\bar{\gamma}}$$
$$\times \exp\left[-\frac{m}{\Omega}\left(\frac{\gamma\xi}{\bar{\gamma}}\right)^{\frac{2}{\alpha}}\right]\left(\frac{\gamma\xi}{\bar{\gamma}}\right)^{\frac{2m}{\alpha}-1} d\gamma. \qquad (41)$$

The equation (41) is written by defining the variable $u = (\gamma\xi/\bar{\gamma})^{\frac{2}{\alpha}}$ as follows

$$P_{\text{out}}(\gamma) \leq \int \frac{m^m}{\Omega\Gamma(m)}\exp\left[-\frac{m}{\Omega}u\right]u^{m-1} du. \qquad (42)$$

Then, it is written with another change of variable $v = u^m$ as

$$P_{\text{out}}(\gamma) \leq \int \frac{m^{m-1}}{\Omega\Gamma(m)}\exp\left[-\frac{m}{\Omega}v^{1/m}\right]dv$$
$$\leq -\frac{\Omega^{m-1}\Gamma\left(m,\frac{m}{\Omega}v^{1/m}\right)}{\Gamma(m)}, \qquad (43)$$

where the integration can be derived by using the equation in [86]. By inverting variables, we obtained the upper bound of the outage probability as follows

$$P_{\text{out}}(\gamma) \leq \Omega^{m-1} - \frac{\Omega^{m-1}\Gamma\left(m,\frac{(\gamma\xi/\bar{\gamma})^{\frac{2}{\alpha}}}{\Omega m^{-1}}\right)}{\Gamma(m)}. \qquad (44)$$

REFERENCES

[1] G. Chen, S. Wu, J. You, and Q. Zhang, "Communication-navigation integrated satellite constellation for lunar exploration: Frozen-orbit based HyInc walker," *IEEE J. Sel. Areas Commun.*, vol. 42, no. 5, pp. 1436–1452, May 2024.

[2] M. Y. Abdelsadek et al., "Future space networks: Toward the next giant leap for humankind," *IEEE Trans. Commun.*, vol. 71, no. 2, pp. 949–1007, Feb. 2023.

[3] S. Liyanaarachchi, S. Mitrolaris, P. Mitra, and S. Ulukus, "6G at $\frac{1}{6}g$: The future of cislunar communications," 2024, *arXiv:2407.16672*.

[4] A. Burg, E. McVay, and D. Reeves, "Architecture robustness in NASA's moon to mars capability development—FY23 data results," in *Proc. IEEE Aerosp. Conf.*, 2023, pp. 1–14.

[5] (NASA, Washington, DC, USA). *Moon-to-Mars Architecture Definition Document: STI Program Report Series*. Apr. 2023. [Online]. Available: https://ntrs.nasa.gov/citations/20230002706

[6] A. Yuan, Z. Hu, Q. Zhang, Z. Sun, and Z. Yang, "Toward the age in cislunar communication: An AoI-optimal multi-relay constellation with heterogeneous orbits," *IEEE J. Sel. Areas Commun.*, vol. 42, no. 5, pp. 1420–1435, May 2024.

[7] P. Kessler, T. Prater, T. Nickens, and D. Harris, "Artemis deep space habitation: Enabling a sustained human presence on the moon and beyond," in *Proc. IEEE Aerosp. Conf.*, 2022, pp. 1–12.

[8] *NASA's Lunar Exploration Program Overview*, NASA, Washington, DC, USA, Sep. 2020.

[9] A. Balossino and F. Davarian, "The moon needs decent wireless coverage: Argotec and JPL's relay satellites could deliver bandwidth for more than 90 missions," *IEEE Spectr.*, vol. 59, no. 4, pp. 32–37, Apr. 2022.

[10] S. Gecgel Cetin, G. Karabulut Kurt, and A. Vazquez Castro, "Secure and robust communications for cislunar space networks," in *Proc. 40th Int. Commun. Satell. Syst. Conf.*, 2023, pp. 45–52.

[11] N. Benchoubane, B. Donmez, O. Ben Yahia, and G. K. Kurt, "Securing cislunar missions: A location-based authentication approach," in *Proc. Security Space Syst.*, 2024, pp. 1–8.

[12] N. G. Gordon, D. Marsili, I. Nikas, and N. Boschetti, "Lasers on the moon: Recommendations for pioneering lunar communication infrastructure," *IEEE Pervasive Comput.*, vol. 22, no. 2, pp. 19–25, Apr.–Jun. 2023.

[13] *The Future Lunar Communications Architecture: Lunar Communications Architecture Working Group*, Interag. Oper. Advis. Group, Washington, DC, USA, Jan. 2022.

[14] *International Communication System Interoperability Standards (ICISIS)*, Nat. Aeronaut. Space Admin., Washington, DC, USA, State Space Corp. ROSCOSMOS, Moscow, Russia, Eur. Space Agency, Paris, France, Can. Space Agency, Longueuil, QC, Canada, Minist. Educ., Culture, Sports, Sci. Technol., Tokyo, Japan, Mar. 2019.

[15] G. Xu and Z. Song, "Effects of solar scintillation on deep space communications: Challenges and prediction techniques," *IEEE Wireless Commun.*, vol. 26, no. 2, pp. 10–16, Apr. 2019.

[16] G. Xu and Q. Zhang, "Mixed RF/FSO deep space communication system under solar scintillation effect," *IEEE Trans. Aerosp. Electron. Syst.*, vol. 57, no. 5, pp. 3237–3251, Oct. 2021.

[17] B. Bala, L. J. Lanzerotti, D. E. Gary, and D. J. Thomson, "Noise in wireless systems produced by solar radio bursts," *Radio Sci.*, vol. 37, no. 2, pp. 1–7, Apr. 2002.

[18] C. M. Ho, D. D. Morabito, and R. Woo, "Solar corona effects on angle of arrival fluctuations for microwave telecommunication links during superior solar conjunction," *Radio Sci.*, vol. 43, no. 2, pp. 1–13, Apr. 2008.

[19] Q. Rao, G. Xu, and Z. Zheng, "The effects of dust particle radius on the propagation characteristics of THz wave in a dusty plasma slab," in *Proc. Int. Conf. Microw. Millim. Wave Technol.*, 2021, pp. 1–3.

[20] D. D. Morabito, D. Buccino, and D. Kahan, "An analysis of Juno downlink Ka-band Carrier data," NASA Jet Propuls. Lab., California Inst. Technol., Pasadena, CA, USA, Rep. 42-237, May 2024. [Online]. Available: https://ipnpr.jpl.nasa.gov/progress_report/42-237/42-237B.pdf

[21] D. S. Kahan, D. R. Buccino, W. A. Majid, R. Navarro, J. B. Berner, and B. W. Arnold, "Radio frequency interference impacting the martian X-band radio environment," NASA Jet Propuls. Lab., California Inst. Technol., Rep. 42-230, Aug. 2022. [Online]. Available: https://ipnpr.jpl.nasa.gov/progress_report/42-230/42-230B.pdf

[22] "DSN telecommunications link design handbook," Jet Propuls. Lab. California Inst. Technol., Rep. 810-005, 2000. [Online]. Available: https://deepspace.jpl.nasa.gov/dsndocs/810-005/

[23] L. Carrer, D. M. Schroeder, A. Romero-Wolf, P. Ries, and L. Brurzone, "Noise character constraints on passive radio sounding of Jupiter's icy moons using Jovian decametric radiation," in Proc. IEEE Int. Geosci. Remote Sens. Symp., 2018, pp. 4158–4161.

[24] C. Watson et al., "Radio instrument package for lunar ionospheric observation: A concept study," Radio Sci., vol. 58, no. 7, pp. 1–15, Jul. 2023.

[25] "Unique science from the moon in the artemis era," Nat. Aeronaut. Space Admin., Washington, DC, USA, document NESC-RP-22-01729, Feb. 2022.

[26] Z. Huang and J. Wang, "Modeling lunar surface charging under space weather conditions derived from the ARTEMIS and OMNI data," IEEE Trans. Plasma Sci., vol. 51, no. 9, pp. 2515–2521, Sep. 2023.

[27] P. Song et al., "Feasibility study of a high-resolution shallow surface penetration radar for space application," Radio Sci., vol. 56, no. 2, pp. 1–20, Feb. 2021.

[28] Y. Zhao, T. Zhang, X. Wu, and H. Zhang, "Control strategy of lunar lander-relay satellite antenna acquisition and tracking for Chang'e-4 lunar exploration mission," in Proc. IEEE Conf. Ind. Electron. Appl., 2020, pp. 1506–1510.

[29] R. Rugani, F. Martelli, M. Martino, and G. Salvadori, "Moon village: Main aspects and open issues in lunar habitat thermoenergetics design. A review," in Proc. IEEE Int. Conf. Environ. Elect. Eng. IEEE Ind. Commer. Power Syst. Eur., 2021, pp. 1–6.

[30] N. S. Mohamad and K. Chellappan, "The relationship between total electron content (TEC), tides phenomena and the position of moon and sun during the full moon and new moon in Selangor," in Proc. Int. Conf. Space Sci. Commun., 2015, pp. 277–282.

[31] N. Liu and Y.-Q. Jin, "Simulation and data analysis of the temperature distribution and variation in the permanent shaded region of the moon," IEEE Trans. Geosci. Remote Sens., vol. 59, no. 4, pp. 2962–2972, Apr. 2021.

[32] Z. Meng et al., "Constructing a complete brightness temperature dataset of the moon with Chang'e-2 microwave radiometer data," IEEE Trans. Geosci. Remote Sens., vol. 61, 2023, Art. no. 5302114.

[33] J. M. Tejeda, P. Fajardo, M. K. Verma, and C. Verhoeven, "The complete set of thermo-mechanical-radiation methods, simulations and results for a swarm of nanorovers deployed on the moon's surface (Lunar Zebro mission)," Adv. Astronaut. Sci. Technol., vol. 5, no. 4, pp. 317–224, 2022.

[34] T.-Y. Park, J.-J. Lee, J.-H. Kim, and H.-U. Oh, "Preliminary thermal design and analysis of lunar lander for night survival," Int. J. Aerosp. Eng., vol. 2018, pp. 1–13, Oct. 2018.

[35] T. Oikawa1 et al., "Thermal design and analysis of conceptual flight model for a lunar exploration rover," in Proc. Int. Symp. Artif. Intell., Robot. Autom. Space, 2016, pp. 1–12.

[36] G.-P. Hu et al., "Brightness temperature of the global moon: Comparison between theoretical simulation and observation by Chang'e-1 lunar orbiter," in Proc. Int. Conf. Microw. Millim. Wave Technol., 2010, pp. 1735–1738.

[37] D. D. Morabito, W. Imbriale, and S. Keihm, "Observing the moon at microwave frequencies using a large-diameter deep space network antenna," IEEE Trans. Antennas Propag., vol. 56, no. 3, pp. 650–660, Mar. 2008.

[38] D. Morabito, "Lunar noise-temperature increase measurements at S-band, X-band, and Ka-band using a 34-meter-diameter beam-waveguide antenna," NASA Jet Propuls. Lab., California Inst. Technol., Pasadena, CA, USA, Rep. 42-166, Aug. 2006. [Online]. Available: https://tmo.jpl.nasa.gov/progress_report/42-166/166C.pdf

[39] E. Serria et al., "A review of lunar communications and antennas: Assessing performance in the context of propagation and radiation," Sensors, vol. 23, no. 24, p. 9832, 2023.

[40] J.-P. Williams et al., "Seasonal polar temperatures on the moon," J. Geophys. Res., Planets, vol. 124, no. 10, pp. 2505–2521, 2019.

[41] B. Donmez and G. K. Kurt, "Continuous power beaming to lunar far side from EMLP-2 halo orbit," 2024, arXiv:2402.16320.

[42] M. S. Net, N. Rodriguez Alvarez, D. Kahan, D. Morabito, and H. Elliott, "Multipath measurements at the lunar south pole from opportunistic ground-based observations—Part I: Experiment concept," NASA Jet Propuls. Lab., California Inst. Technol., Pasadena, CA, USA, Rep. 42-222, Aug. 2020.

[43] N. R. Alvarez, M. S. Net, D. Kahan, D. Morabito, and H. Elliott, "Multipath measurements at the lunar south pole from opportunistic ground-based observations—Part II: Experiment results," NASA Jet Propuls. Lab., California Inst. Technol., Pasadena, CA, USA, Rep. 42-222, Aug. 2021.

[44] M. S. Net, "Simulation of multipath reflections from planetary bodies: Theory and application to the lunar south pole," NASA Jet Propuls. Lab., California Inst. Technol., Pasadena, CA, USA, Rep. 42-226, Aug. 2021. [Online]. Available: https://tmo.jpl.nasa.gov/progress_report/42-216/42-216C.pdf

[45] M. S. Net and K.-M. Cheung, "Mitigating fading in cislunar communications: Application to the human landing system," in Proc. IEEE Aerosp. Conf., 2020, pp. 1–11.

[46] R. C. Toonen, S. L. Booth, B. W. Welch, and M. J. Zemba, "Optimizing lunar map partitioning for multipath fade loss analyses," IEEE J. Radio Freq. Identif., vol. 6, pp. 284–291, Mar. 2022.

[47] M. S. Net, "Analysis of the fading channel in downlinks from the lunar south pole to the deep space network," NASA Jet Propuls. Lab., California Inst. Technol., Pasadena, CA, USA, Rep. 42-216, Feb. 2019. [Online]. Available: https://tmo.jpl.nasa.gov/progress_report/42-216/42-216C.pdf

[48] D. Divsalar, M. S. Net, and K.-M. Cheung, "Acquisition and tracking for communications between lunar south pole and Earth," in Proc. IEEE Aerosp. Conf., 2019, pp. 1–14.

[49] D. Divsalar, M. S. Net, and K. M. Cheung, "Comparing performance of coded communications over fading channels between the lunar south pole & Earth," in Proc. IEEE Aerosp. Conf., 2022, pp. 1–11.

[50] S. J. Keihm, "Effects of subsurface volume scattering on the lunar microwave brightness temperature spectrum," Icarus, vol. 52, no. 3, pp. 570–584, 1982.

[51] R. Dendy, D. Mortensen, D. Zeleznikar, and S. Booth, "Flexible user radio for Lunar missions," in Proc. IEEE Aerosp. Conf., 2023, pp. 1–11.

[52] Y. Matsumoto, R. Nakamura, D. Goto, J. Kikuchi, M. Hidaka, and S. Ueda, "An efficient search scheme for using weak stability boundary in a backup scenario of NRHO transfer," in Proc. IEEE Aerosp. Conf., 2022, pp. 1–9.

[53] J. Li et al., "Hierarchical communication architecture and network protocol for cislunar constellation," in Proc. IEEE Int. Conf. Adv. Infocomm Technol., 2023, pp. 125–131.

[54] C. Liu, Y. Su, and J.-F. Zhou, "An interference model for low frequency radio spectrometer onboard Chang'e-4 mission," Radio Sci., vol. 58, no. 3, pp. 1–9, Mar. 2023.

[55] Q. He, Q. Liu, and X. Zheng, "Chang'e-3 spacecraft surface reflection causes turbulence on VLBI delay," Radio Sci., vol. 52, no. 2, pp. 235–247, Feb. 2017.

[56] J. Griffin, "Noise pedestal effects in turnaround ranging channels on conscan performance," NASA Jet Propuls. Lab., California Inst. Technol., Pasadena, CA, USA, Rep. 42-227, Nov. 2021. [Online]. Available: https://ipnpr.jpl.nasa.gov/progress_report/42-227/42-227A.pdf

[57] M. S. Net, "Effect of hot body noise sources on arrays of deep space network antennas," NASA Jet Propuls. Lab., California Inst. Technol., Pasadena, CA, USA, Rep. 42-235, Nov. 2023. [Online]. Available: https://ipnpr.jpl.nasa.gov/progress_report/42-235/42-235A.pdf

[58] Q. He, "Investigation on peculiar SNR variation at TianMa radio telescope," Sci. Rep., vol. 9, Dec. 2019, Art. no. 18421.

[59] A. Chopra and B. L. Evans, "Outage probability for diversity combining in interference-limited channels," IEEE Trans. Wireless Commun., vol. 12, no. 2, pp. 550–560, Feb. 2013.

[60] K. Gulati, B. L. Evans, J. G. Andrews, and K. R. Tinsley, "Statistics of co-channel interference in a field of poisson and poisson-poisson clustered interferers," *IEEE Trans. Signal Process.*, vol. 58, no. 12, pp. 6207–6222, Dec. 2010.

[61] J. Ilow and D. Hatzinakos, "Analytic α-stable noise modeling in a poisson field of interferers or scatterers," *IEEE Trans. Signal Process.*, vol. 46, no. 6, pp. 1601–1611, Jun. 1998.

[62] J. S Seo, S. J Cho, and K. Feher, "Impact of non-Gaussian impulsive noise and multipath fading on the performance of digital mobile-satellite systems," *IETE J. Res.*, vol. 36, no. 1, pp. 50–54, 1990.

[63] C. Zheng, M. Egan, L. Clavier, T. Pedersen, and J.-M. Gorce, "Linear combining in dependent α-stable interference," in *Proc. IEEE Int. Conf. Commun.*, 2020, pp. 1–6.

[64] M. Egan, L. Clavier, M. de Freitas, L. Dorville, J.-M. Gorce, and A. Savard, "Wireless communication in dynamic interference," in *Proc. IEEE Global Commun. Conf.*, 2017, pp. 1–6.

[65] A. Rajan and C. Tepedelenlioglu, "Diversity combining over Rayleigh fading channels with symmetric α-stable noise," *IEEE Trans. Wireless Commun.*, vol. 9, no. 9, pp. 2968–2976, Sep. 2010.

[66] A. Mahmood, M. Chitre, and M. Armand, "PSK communication with passband additive symmetric α-stable noise," *IEEE Trans. Commun.*, vol. 60, no. 10, pp. 2990–3000, Oct. 2012.

[67] J. Wang, E. E. Kuruoglu, and T. Zhou, "α-Stable channel capacity," *IEEE Commun. Lett.*, vol. 15, no. 10, pp. 1107–1109, Oct. 2011.

[68] J. Fahs and I. Abou-Faycal, "On the single-user capacity of some multiple access channels," in *Proc. Int. Symp. Wireless Commun. Syst.*, 2014, pp. 622–627.

[69] J. Fahs and I. Abou Faycal, "On the capacity of additive white alpha-stable noise channels," in *Proc. IEEE Int. Symp. Inf. Theory*, 2012, pp. 294–298.

[70] M. De Freitas, M. Egan, L. Clavier, A. Savard, and J.-M. Gorce, "Power control in parallel symmetric α-stable noise channels," in *Proc. IEEE Int. Workshop Signal Process. Adv. Wireless Commun.*, 2019, pp. 1–5.

[71] M. L. de Freitas, M. Egan, L. Clavier, A. Goupil, G. W. Peters, and N. Azzaoui, "Capacity bounds for additive symmetric α-stable noise channels," *IEEE Trans. Inf. Theory*, vol. 63, no. 8, pp. 5115–5123, Aug. 2017.

[72] T. S. Han, *Channel Coding*. Berlin, Germany: Springer, 2003, pp. 169–268.

[73] G. Samorodnitsky and M. Taqqu, *Stable Non-Gaussian Random Processes: Stochastic Models With Infinite Variance* (Stochastic Modeling Series). Oxfordshire, U.K.: Taylor Francis, 1994.

[74] A. R. Kerr and J. Randa, "Thermal noise and noise measurements— A 2010 update," *IEEE Microw. Mag.*, vol. 11, no. 6, pp. 40–52, Oct. 2010.

[75] A. Kerr, "Suggestions for revised definitions of noise quantities, including quantum effects," *IEEE Trans. Microw. Theory Techn.*, vol. 47, no. 3, pp. 325–329, Mar. 1999.

[76] M. Reid, *Low-Noise Systems in the Deep Space Network* (JPL Deep-Space Communications and Navigation Series). Hoboken, NJ, USA: Wiley, 2008.

[77] J. Kraus and R. Marhefka, *Antennas for All Applications* (McGraw-Hill Series in Electrical Engineering). New York, NY, USA: McGraw-Hill, 2002.

[78] International Telecommunications Union, *Handbook on Satellite Communications*, 3rd ed. Nashville, TN, USA: Wiley, Apr. 2002.

[79] H.-C. Yang and M. Alouini, *Order Statistics in Wireless Communications: Diversity, Adaptation, and Scheduling in MIMO and OFDM Systems*, 1st ed. Cambridge, U.K.: Cambridge Univ., 2011.

[80] A. Goldsmith and P. Varaiya, "Capacity of fading channels with channel side information," *IEEE Trans. Inf. Theory*, vol. 43, no. 6, pp. 1986–1992, Nov. 1997.

[81] M. Bittinger, D. Ellenbogen, and S. Surgent, *Calculus and Its Applications: Expanded Version: Media Update*. London, U.K.: Pearson Educ., 2016.

[82] "Dynamic radioisotope power system (DRPS) design reference mission (DRM) lunar rover," Glenn Res. Center, Nat. Aeronaut. Space Admin., Washington, DC, USA, Rep. CD-2021-182, Oct. 2022.

[83] Space Frequency Coordination Group, *Recommendation SFCG 32-2R5: Communication and Positioning, Navigation, and Timing Frequency Allocations and Sharing in the Lunar Region*, Interag. Oper. Advis. Group, Washington, DC, USA, Jun. 2023.

[84] (Wolfram Res. Inc., Champaign, IL, USA). *MeijerG*. 1996. [Online]. Available: http://functions.wolfram.com/07.34.21.0013.01

[85] Y. Brychkov, O. Marichev, and N. Savischenko, *Handbook of Mellin Transforms*, Boca Raton, FL, USA: CRC Press, 2018.

[86] (Wolfram Res. Inc., Champaign, IL, USA). *Exp*. 1996. [Online]. Available: http://functions.wolfram.com/01. 03.21.0046.01

SELEN GECGEL CETIN (Member, IEEE) received the B.S. degree in electronics and communication engineering from Yildiz Technical University, Istanbul, Türkiye, in 2016, and the M.S. degree in telecommunication engineering from Istanbul Technical University (ITU), Istanbul, in 2019, where she is currently pursuing the Ph.D. degree. From 2019 to 2021, she was a Research Assistant with the Electronic Engineering Department, Turkish Air Force Academy. She is a member of the Wireless Communication Research Laboratory, ITU, and the Poly-Grames Research Center, Polytechnique Montréal. Her current research interests are machine learning, wireless communications, and space networks.

ÁNGELES VAZQUEZ-CASTRO (Senior Member, IEEE) received the M.Sc. and Ph.D. degrees in electrical engineering from the University of Vigo, Spain, in 1994 and 1998, respectively. She was affiliated with the University Carlos III of Madrid until 2002. From 2002 to 2004, she served as a Research Fellow with European Space Agency, Noordwijk, The Netherlands. From 2008 to 2012, she was a Part-Time Visiting Professorship with the University of Oslo, Norway. Since 2004, she has been an Associate Professor with the Universitat Autònoma de Barcelona and a member of the Institute of the Space Studies of Catalonia (IEEC-UAB). Her research focuses on secure space and outer space communications and networking.

GUNES KARABULUT KURT (Senior Member, IEEE) received the Ph.D. degree in electrical engineering from the University of Ottawa, ON, Canada. She is a Canada Research Chair (Tier 1) in New Frontiers in Space Communications and a Professor with Polytechnique Montréal, Montreal, QC, Canada. She is also an Adjunct Research Professor with Carleton University, ON, Canada. She has received the Turkish Academy of Sciences Outstanding Young Scientist (TÜBA-GEBIP) Award in 2019. She is a Marie Curie Fellow.